Solid State Phenomena
ISSN: 1662-9779, Vol. 388, pp 199-207
doi:10.4028/p-0djtbH

Submitted: 2026-01-19
Revised: 2026-02-12
Accepted: 2026-02-21
Online: 2026-04-15

Automated Testing and Calibration of Sheet Metal Models

NDIRITU Clement[1,a*], HAOUES Yasmine[1,b], DECULTOT Nicolas[1,c] and THUILLIER Sandrine[1,d]

[1]Univ. Bretagne Sud, UMR CNRS 6027, IRDL, F-56100 Lorient, France

[a]clement.ndiritu@univ-ubs.fr, [b]yasmine.haoues@univ-ubs.fr, [c]nicolas.decultot@univ-ubs.fr, [d]sandrine.thuillier@univ-ubs.fr

Keywords: Automated Mechanical Testing, Inverse Model Calibration, Anisotropy, Hardening

Abstract. The efficient development of high-quality sheet metal components increasingly depends on predictive numerical simulations conducted prior to forming operations. Achieving such accuracy requires precise calibration of constitutive material models that represent the complex mechanical behaviour of metals. Mechanical testing provides the essential data for calibration, revealing material anisotropy, strain hardening, and ductile fracture. However, traditional characterisation approaches are often labor-intensive, time-consuming, and prone to operator variability. Within the phenomenological framework, numerous tests are typically required to capture the full material response, including repeats for statistical reliability, leading to high costs, extended lead times, and data management challenges. To address these limitations, this study introduces an automated mechanical testing platform designed to rapidly acquire experimental data useful for material models. Robotic automation enables fully automated test sequences, ensuring high repeatability and reducing manual intervention. When combined with automated model calibration, this approach provides a direct link between the physical material (metallic sheet) and its virtual mechanical representation.

Introduction

A primary objective of mechanical testing is to generate data for model calibration, namely the identification of constitutive parameters used in finite element simulations. From experimental databases either based on homogeneous [1] or heterogeneous tests [2], repeatability must be assessed to select representative tests and quantify their reliability, prior to inverse identification. While the selection of mechanical models and associated tests is still largely performed manually, it can be integrated into an automated strategy [3]. When combined with automated testing and post-processing, such an approach could lead to a fully automated workflow, from material testing to parameter identification. To the authors' knowledge, this concept has not yet been realized and constitutes the objective of the AutoMeCal project. As an initial step, this work focuses on mechanical testing for the identification of hardening, anisotropy and uncoupled fracture criteria. These are traditionally identified in two stages: first, hardening and anisotropy are calibrated using uniaxial tensile tests at various orientations and hydraulic bulge tests; second, fracture criteria are calibrated using notched or holed specimens tested up to rupture [4]. Since rupture tests reach high strain levels, extrapolation of the hardening law is often required to fit the load evolution, using either linear [4] or more advanced extrapolation schemes [5]. This motivates the inclusion of rupture tests within the calibration database and the simultaneous identification of anisotropy and hardening parameters over the full experimental dataset [6].

The need for large and repeatable experimental databases has motivated the development of automated mechanical testing systems. An early example includes a robot-assisted testing setup for miniaturized irradiated samples with a thickness of 0.2 mm [7], although no mechanical output signals were reported. More recently, fully or semi-automated tensile testing systems incorporating robotic handling, laser-based dimensional measurements, and digital image correlation have been proposed [8, 9]. These studies demonstrate the ability to perform large numbers of tests, up to 77 and 360, respectively, highlighting the potential of automated testing for generating extensive experimental databases required to characterize material behaviour under multiple loading states.

The aim of this paper is to present the first results obtained within a quasi-automated approach, for a third-generation steel Fortiform®1050, of thickness 0.85 mm. Homogeneous tensile tests at 5 orientations to the rolling direction were performed with an automated testing system developed on purpose, as well as rupture tests on specimens with notches and holes. An isotropic hardening model coupled with the anisotropic yield criterion Yld2004-18p [10] is considered and material parameters are identified, adding a previously performed hydraulic bulge test result. The final aim would be to calibrate an uncoupled rupture criterion; however, only hardening and anisotropy are considered in a first step. Though the whole procedure is not yet fully automatic, this study presents the first steps of an integrated fully automatic procedure.

Material and Methods

Automated testing platform.

An automated experimental platform was developed to perform series of tensile and rupture tests with minimal human intervention. The main objective of this system is to ensure high repeatability, reduce operator-dependent variability, and enable the rapid acquisition of experimental data suitable for constitutive model calibration.

The platform integrates three main components: (i) an automated uniaxial tensile testing machine developed by MatAndSim, (ii) a six-degree-of-freedom collaborative robotic manipulator for specimen handling from Universal Robots (UR3) and (iii) a stereo digital image correlation (DIC) system for full-field strain measurements from MatchID, see Fig. 1.

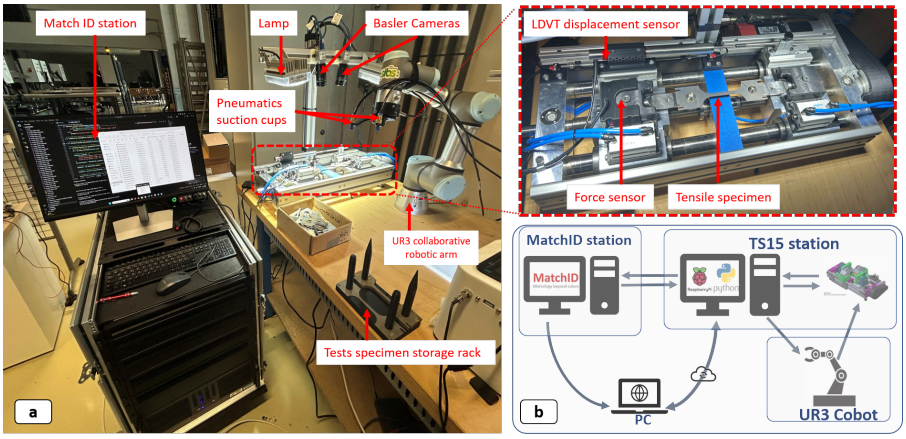

Fig. 1: (a) Automated mechanical testing platform (b) Schematic diagram of the main components of the automatic testing platform. TS15 is developed by MatAndSim (`https://matandsim.fr/`)

The tensile testing machine (TS15) is a horizontal uniaxial device with a maximum load capacity of 15 kN. It is based on a parallel configuration with two grips moving symmetrically in opposite directions. The applied force is measured using a calibrated load cell, while displacement is monitored by a linear variable differential transformer (LVDT) and an internal position sensor. The testing machine is operated as an automated unit controlled by an embedded computer (Raspberry Pi), which executes the predefined loading sequences. Mechanical signals are acquired through an external data acquisition board (LabJack) and transmitted to the main controller. Test parameters such as displacement rate, loading path, and test duration are defined prior to testing and executed automatically. Load and displacement are recorded continuously throughout the test.

Specimen handling is performed using a collaborative robotic arm (UR3) with a positioning accuracy of ± 0.1mm. The robot automatically retrieves specimens from a storage system and places them onto the cylindrical rods (pins) of the TS15 tensile testing machine. A pneumatic gripping system equipped with suction cups is used to handle the specimens reliably while limiting surface damage.

All specimens incorporate holes at each end to enable pin loading and create a pinned connection. This configuration ensures symmetric uniaxial loading while allowing rotational freedom at the grips, thereby minimizing eccentric loading and bending effects. After completion of the test, the robot automatically removes the loaded or fractured specimen. This robotic setup enables fully automated test sequences for several specimen geometries.

Full-field strain measurements are obtained using a stereo digital image correlation (DIC) system (MatchID) comprising two synchronized high-resolution Basler cameras (Basler ace 2 a2A4096-30umPRO) observing the specimen gauge section throughout the loading sequence. Prior to testing, a stereo calibration using a dedicated target is performed to identify the intrinsic and extrinsic camera parameters, after which the setup remains fixed; this is achieved by leveraging the MatchID Calib package.

Mechanical testing is executed via an automated control script on the TS15 system, which controls the loading sequence and triggers image acquisition through hardware synchronization leveraging the MatchID Grabber package. Image acquisition is fully synchronized with the mechanical loading, and images are recorded together with their corresponding time information. Post-processing is automatically initiated using a Python script that launches MatchID Stereo package. On a predefined region of interest (ROI) on the reference image, stereo correlation is performed to compute displacement fields and subsequently strains. Displacement and strain fields are extracted using Python-based routines and combined with the force and displacement data recorded by the TS15 controller.

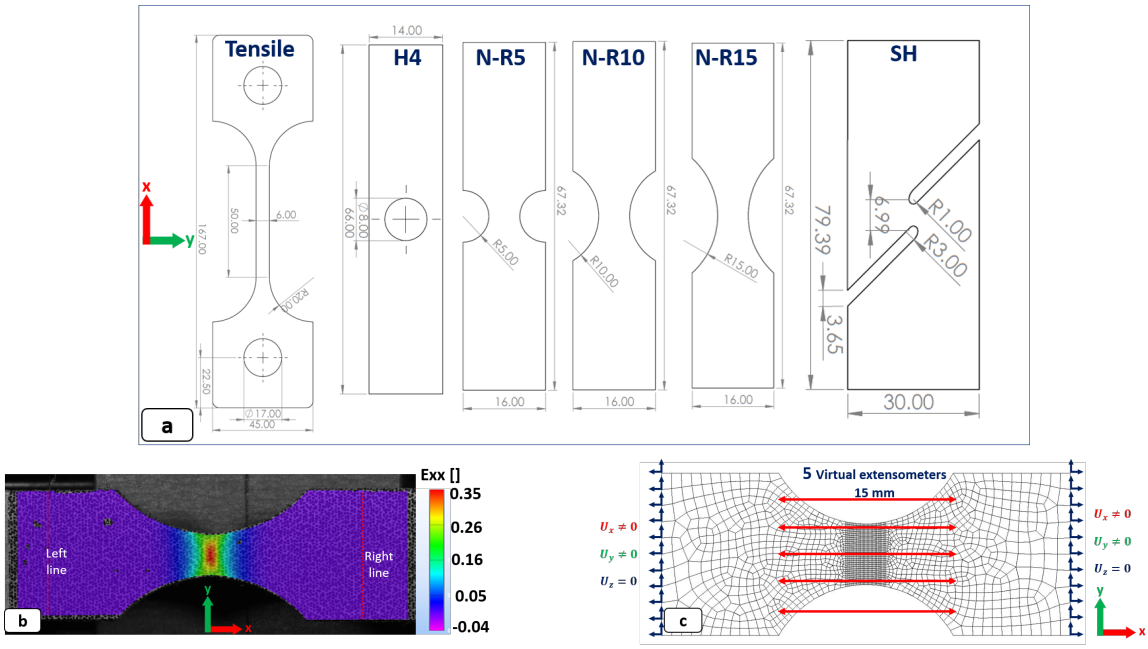

Fig. 2: (a) Geometries of the tensile and ductile fracture tests. The extremities of the uniaxial tensile test specimen include a larger-width region with a hole, used to pull the sample. For the rupture tests, a similar region exists but is not shown here. (b) DIC image obtained on N-R15 test. The two red lines highlight the position where displacements for FE simulations are output (c) Boundary conditions (BCs) representing experimental conditions as extracted from DIC image.

Mechanical tests.

All test specimens were machined from the same sheet using a CNC water jet cutting machine, and their dimensions were measured prior to testing to verify machining accuracy. Standard dog-bone specimens with a width of 6 mm were designed according to ISO 6892-1 for monotonic tensile testing. These specimens were machined along the rolling direction (RD) as well as at 22.5°, 45°, 67.5°, and 90° relative to RD to investigate coupled hardening and anisotropy. In addition, five ductile fracture specimen geometries, machined exclusively along RD, were selected to generate a wide range of stress

states. Notched specimens with small (N-R5), medium (N-R10), and large (N-R15) notch radii were employed to achieve a high stress triaxiality. A specimen with a central hole (H-R4) was used to approach a uniaxial stress state while limiting necking, and a shear-type specimen (SH) was selected to obtain low stress triaxiality [11, 5].

For each specimen geometry and loading direction, three to five samples were prepared to assess experimental repeatability. Specimen surfaces were prepared manually for digital image correlation (DIC) by cleaning and applying a white base coat, followed by a stochastic black speckle pattern generated using the MatchID speckle generator and printed with an ArtisJet UV printer. Specimens were placed on a storage rack.

All tests except the hydraulic bulge test were conducted on the automated testing platform. The crosshead speed and displacement limits were defined individually for each fracture specimen type via a configuration file, while identical parameters were used for all uniaxial tensile tests. Image acquisition for both tensile and fracture tests was performed using the MatchID Grabber with identical camera calibration settings. Among the five tests conducted for each specimen geometry, at least two showed closely matching responses; one representative test was selected based on minimal experimental uncertainty, highlighting the potential influence of specimen misalignment.

Image correlation was conducted on predefined ROIs using the MatchID stereo DIC system in batch mode, automatically triggered via a Python script after each acquisition. For uniaxial tensile tests, the Cauchy stress was computed as the applied force divided by the current cross-sectional area prior to necking, while logarithmic strain components were evaluated in a homogeneous region of interest using the Euler strain convention with a subset size of 43 pixels, a step size of 8 pixels, and a strain window of 4 pixels. Lateral and transverse strains were automatically extracted for each correlated image. For fracture tests, displacements were obtained using predefined virtual extensometers within selected correlation regions. Five extensometers with a gauge length of 15 mm were positioned at different specimen locations to evaluate potential misalignment effects, and the averaged displacement was used for material identification. The fracture displacement, u_f, was defined as the mean displacement at the fracture time t_f, identified by a sudden drop in the force–displacement curve.

To enable subsequent numerical simulations of the fracture tests, it is essential to accurately reproduce the experimental displacement boundary conditions, as these have been shown to significantly influence the calibration of ductile fracture models compared to idealized boundary conditions [5]. Accordingly, two perpendicular lines, as shown in Fig. 2b, were predefined across each fracture specimen within the automated post-processing script. Displacements were projected onto the best-fit plane of the correlated surface to extract the temporal evolution of the displacement components along the loading direction, U_x [mm], and the transverse direction, U_y [mm], at each point along the defined lines.

Constitutive modelling.

An elastoplastic constitutive law with isotro- pic hardening and the anisotropic yield criterion yld2004-18p [10] is used in this study. The yield criterion is written as:

$$\phi = \sum_{i=1,j=1}^{3} \left| \widetilde{S}_i^{(1)} - \widetilde{S}_j^{(2)} \right|^a = 4{\sigma_y}^a \quad \text{with} \quad \widetilde{S}^{(k)} = \widetilde{L}^{(k)} : S \ , \ \ k = 1, 2, \tag{1}$$

with

$$\widetilde{L}^{(k)} = \begin{bmatrix} 0 & -c_{12}^{(k)} & -c_{13}^{(k)} & 0 & 0 & 0 \\ -c_{21}^{(k)} & 0 & -c_{23}^{(k)} & 0 & 0 & 0 \\ -c_{31}^{(k)} & -c_{32}^{(k)} & 0 & 0 & 0 & 0 \\ 0 & 0 & 0 & c_{44}^{(k)} & 0 & 0 \\ 0 & 0 & 0 & 0 & c_{55}^{(k)} & 0 \\ 0 & 0 & 0 & 0 & 0 & c_{66}^{(k)} \end{bmatrix}, \ \ k = 1, 2$$

with σ_y the yield stress and S the deviatoric part of Cauchy stress tensor. The exponent a is fixed to the value of 6 for body-centered cubic materials. As no information is available for shear in the thickness directions, parameters $c_{44}^{(k)}$ and $c_{55}^{(k)}$, $k = 1, 2$, are fixed equal to 1, leading to a total of 14 parameters to identify. Moreover, the combined Swift-Voce equation is used to describe the isotropic hardening,

$$\sigma_y(\bar{\varepsilon}_p) = \alpha \left[A \left(\varepsilon_0 + \bar{\varepsilon}_p\right)^n\right] + (1 - \alpha) \left[\sigma_0 + Q \left(1 - exp \left(-b\bar{\varepsilon}_p\right)\right)\right] \tag{2}$$

where $\bar{\varepsilon}_p$ is the equivalent plastic strain and α, A, ε_0, n, σ_0, Q and b are the material parameters to identify.

Numerical models.

The mechanical tests were simulated in three dimensions using the finite element (FE) code *ABAQUS*® within an implicit framework. Homogeneous tensile tests were modeled using a three-dimensional unit element, whereas ductile fracture tests were simulated with full specimen models to capture material heterogeneity. Only the specimen portion between the pin-connection holes was modeled, such that the FE specimen length matched the distance between the two predefined vertical lines used to extract the experimental displacement.

All specimens were discretized using three-dimensional reduced-integration hexahedral elements (C3D8R), with the default total-stiffness hourglass control in *ABAQUS*®. A locally refined mesh with an element size of approximately 0.1 mm was employed in regions of expected strain localization, while coarser elements were used for boundary condition application. Based on a convergence study of the fracture strain, which showed convergence for meshes with more than six elements through the thickness [5]. Therefore, three elements were used to model the symmetry.

Displacement boundary conditions with non-zero components (U_x, U_y) were applied to the left and right specimen edges, as shown in Fig. 2, together with a symmetry boundary condition in the thickness direction. An automated Python-based procedure was developed to impose the displacement boundary conditions on 11 nodal regions of the FE model for each fracture test, as illustrated in Fig. 2. This approach leads to a more realistic representation of experimental conditions by accounting for specimen misalignment effects observed during testing [5].

Five virtual extensometers were defined at the same locations as in the DIC analysis to extract local displacements for plotting load evolution. For ductile fracture tests, differences in filtering and spatial resolution between DIC and FE data typically require a levelling procedure, whereby FE results are post-processed using the same filters as the experimental data. Since this procedure was not applied in the present study, only the global force–displacement response was used for material parameter identification. The mechanical behaviour was modeled using a user-defined material subroutine [1].

Material parameter identification.

The 21 material parameters introduced in the modelling section govern hardening and anisotropy based on experimental data spanning a wide strain range of up to approximately 0.4. The diversity of tests included in the identification database enabled the characterisation of hardening behaviour over large deformations, overcoming the limitations of linear piecewise hardening laws obtained through manual inverse methods based on iterative visual fitting. However, a hydraulic bulge test result, previously obtained, was also considered to add information for the yield criterion calibration. In this study, parameter identification was performed using FEMU, an inverse calibration approach formulated as an optimisation problem that minimizes the discrepancy between experimental measurements and numerical predictions. The framework couples an optimisation algorithm with finite element (FE) simulations and is based on iterative updates of the material parameters. At each iteration, experimental and numerical responses are compared via an objective function $\mathcal{L}(\mathbf{A})$, and the parameter set is updated to progressively reduce the mismatch.

The inverse calibration framework was applied to nine experiments, comprising five homogeneous uniaxial tensile tests, three heterogeneous ductile fracture tests and a hydraulic bulge test. Accordingly, the cost function is decomposed into the following test groups:

$$\mathcal{L}(\mathbf{A}) = \sum_{n=1}^{N} \mathcal{L}_{\text{obj}}^{n}(\mathbf{A}) = \sum_{\alpha} \mathcal{L}_{\text{obj}}^{\text{TU-S}} + \sum_{\alpha} \mathcal{L}_{\text{obj}}^{\text{TU-E}} + \mathcal{L}_{\text{obj}}^{\text{BT}} + \mathcal{L}_{\text{obj}}^{\text{H-R4}} + \mathcal{L}_{\text{obj}}^{\text{N-R5}} + \mathcal{L}_{\text{obj}}^{\text{SH}} \tag{3}$$

where TU-S and TU-E denote the stress level and transverse strain in uniaxial tension, respectively, while BT corresponds to the stress level in hydraulic bulge test at the pole, H-R4, N-R5 and SH correspond to the reaction force evolution in the respective ductile fracture tests. The summation over α accounts for the different orientations with respect to the rolling direction.

The contribution of each test n is defined as

$$\mathcal{L}_{\text{obj}}^{n}(\mathbf{A}) = \frac{1}{n_p^n} \sum_{i=1}^{n_p^n} \left(\frac{Z_i^{\text{exp}}(t_i) - Z_i^{\text{num}}(\mathbf{A})}{W\text{abs}_k} \right)^2, \tag{4}$$

where n_p^n is the number of points for each test n, Z_i^{exp} and Z_i^{num} are the experimental and numerical responses evaluated at time t_i, and $W\text{abs}_k$ is a group-dependent weighting factor used to normalize residuals.

The weighting factors associated with each experimental group are defined as

$$W\text{abs} = \begin{cases} 0.0363, & \text{k = TU-S,} \\ 1.011 \times 10^{-5} & \text{k = TU-E} \\ 0.0432, & \text{k = BT,} \end{cases}, \quad W\text{abs} = \begin{cases} 0.282, & \text{k = H-R4,} \\ 0.263, & \text{k = N-R5,} \\ 0.0956, & \text{k = SH.} \end{cases} \tag{5}$$

This weighting strategy ensures a balanced contribution of stress, strain, and force data in the identification process. Parameter identification is carried out using a Fortran-based interface program coupled with the finite element code *ABAQUS*® for numerical simulations and the optimisation software SdL [11] for iterative parameter updates and convergence control. In SdL, the objective function is minimized using the gradient-based Levenberg–Marquardt (L–M) algorithm. Convergence is achieved when either a stagnation threshold of 1×10^{-7} in the objective function between successive iterations is reached or the maximum number of iterations, limited to 750, is exceeded.

Despite its robustness, the L–M algorithm may converge to local minima depending on the initial parameter values. To reduce this risk, the identification procedure was repeated using three different initial parameter sets.

Results and Discussion

Table 1 shows the initial and optimized values for the three parameter sets, and Fig. 3 illustrates the results for RD, $45°$ and $90°$/RD configurations and Fig. 4 for some rupture tests. As a whole, similar predictions are obtained, though the parameter values are rather different, highlighting the well-known difficulty related to convergence to local minima with gradient-based algorithms. The hardening law based on a combination of Swift-Voce equations, without additional constraints, gives a very large number of possibilities, though the resulting flow stress is rather similar. These results must be strengthened by increasing the number of initial values. Moreover, the hydraulic bulge test is required for the identification, stressing the need to consider identifiability analysis in the procedure. The experimental database could be enriched with the heterogeneous strain fields of the fracture tests, to overcome this issue [2]. However, this integrated calibration shows that the load level in rupture tests is well described, without the need for further adjustments.

Concerning the automated experimental procedure, Table 2 shows what was partially or fully automated and what is still handled manually. The DIC operations must be strengthened, to align the experimental and numerical frames and for data output and comparison with FE results. The calibration procedure was already handled in a semi-automatic way, based on a sequence of operations launched by Python scripts. The main issue in the calibration is the design of relevant indicators for the

Table 1: Identified material parameters for different initial guesses. Ini. and Opti. stand respectively for initial and optimized parameter sets.

	Yield anisotropy parameters														Hardening parameters							$\mathcal{L}(\mathbf{A})$
Set / State	$c_{12}^{(1)}$	$c_{13}^{(1)}$	$c_{21}^{(1)}$	$c_{23}^{(1)}$	$c_{31}^{(1)}$	$c_{32}^{(1)}$	$c_{66}^{(1)}$	$c_{12}^{(2)}$	$c_{13}^{(2)}$	$c_{21}^{(2)}$	$c_{23}^{(2)}$	$c_{31}^{(2)}$	$c_{32}^{(2)}$	$c_{66}^{(2)}$	α	A	ε_0	n	σ_0	Q	b	$\times 10^6$
Set 1 – Ini.	-2.00	-1.80	-1.50	-0.90	-1.20	-0.60	-1.70	-1.30	-1.10	-0.90	-1.40	-0.80	-1.60	-2.00	0.12	1350.00	5.0E-5	0.11	520.00	220.00	6.00	1808
Set 1 – Opti.	-0.67	-0.31	-1.40	-0.55	-1.58	-1.03	-1.32	-0.74	-0.55	-0.83	-1.31	-0.79	-0.99	-0.57	0.13	2690.04	1.81E-5	0.10	766.66	497.73	10.58	6.43
Set 2 – Ini.	0.90	-0.30	1.40	-0.20	0.60	-1.10	0.70	1.30	-0.50	0.90	-0.70	1.10	-0.40	1.50	0.62	2450.00	2.20E-3	0.27	780.00	410.00	19.00	7149
Set 2 – Opti.	0.40	-0.19	1.51	-0.07	0.20	-0.97	0.98	0.61	-0.35	1.17	-1.15	1.29	0.02	1.02	0.55	2014.44	1.76E-3	0.16	898.34	356.69	11.80	6.67
Set 3 – Ini.	1.50	1.00	1.00	1.20	0.20	0.70	1.10	0.20	0.80	1.00	0.40	1.50	0.80	0.30	0.51	1785.42	2.38E-3	0.12	750.37	500.88	23.49	2918
Set 3 – Opti.	1.43	1.65	1.06	0.60	0.37	0.88	1.36	0.16	0.92	0.37	0.76	0.35	0.93	0.21	0.52	2041.94	4.53E-3	0.17	555.17	208.37	20.03	6.85
Lower bound	−2.2														0.1	1300	1.0E-5	0.1	500	200	5	–
Upper bound	2.2														0.9	3200	7.0E-3	0.35	900	800	30	–
Units	–														–	MPa	–	–	MPa	MPa	–	–

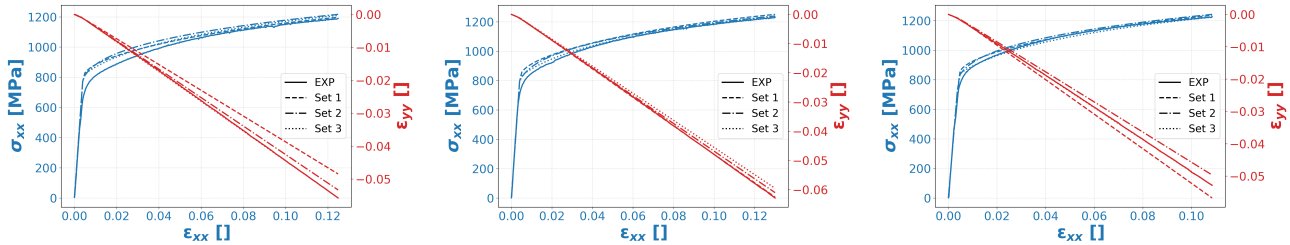

(a) 0°(RD) (b) 45°/RD (c) 90°/RD

Fig. 3: Stress–strain response for tensile tests at different orientations relative to the rolling direction

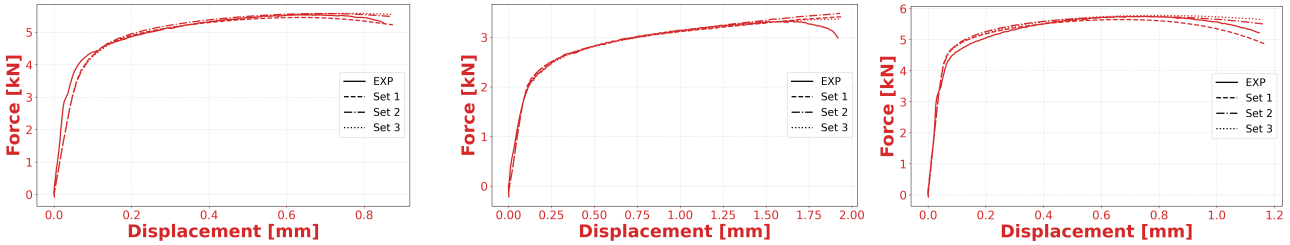

(a) H-R4 (b) SH (c) N-R10

Fig. 4: Force-displacement response for ductile fracture tests: H-R4, SH (in the calibration database) and N-R10 used for the validation

validation of parameter sets. Though the gap between experimental and predicted values is of interest, it is not sufficient and identifiability analysis should be added prior to testing.

Table 2: Summary of the experimental and data-processing steps and their mode within the proposed framework.

Step	Process / Method	Mode
1	Dimensional measurements	Manual
2	Speckle patterning	Manual
3	Sample handling	Automatic
4	Camera calibration	Manual
5	ROI, Virtual extensometer and BCs definition	Manual
6	Image acquisition	Automatic
7	Mechanical testing load acquisition	Automatic
8	DIC, strain calculation and BCs extraction	Automatic
9	Post-processing	Automatic

Conclusions

In this study, an anisotropic plasticity model for a third-generation steel was calibrated using specifically generated experimental data within a semi-automated framework. Dimensional verification, speckle patterning, ROI and sketch definitions, and camera calibration were performed manually, while sample handling, image acquisition, and DIC processing and post-processing were fully automated. Future work will focus on integrating the manual and automated procedures into a unified tool to enable comprehensive and efficient characterisation of sheet metal behaviour, including the calibration of fracture models.

Beyond enabling reliable calibration of anisotropic plasticity models, the proposed experimental and data-processing framework establishes a consistent basis for the subsequent identification of ductile fracture criteria. The automated nature of the approach is particularly suited to generating large, high-quality datasets required for fracture model identification and validation, thereby supporting a more comprehensive description of sheet metal mechanical behaviour.

Acknowledgements

The research leading to these results has received funding from ANR for the project *Automated mechanical lab' and model calibration (AutoMeCal)*, project ANR-23-CE10-0007-01, `https://anr.fr/Project-ANR-23-CE10-0007`. The authors acknowledge MatAndSim for fruitful discussions and their contribution to the automated platform.

References

[1] N. Souto, A. Andrade-Campos and S. Thuillier: Int. J. Mater. Forming Vol. 10 (2017), 353-367

[2] L. Germain, M. Gonçalves, A. Andrade-Campos and S. Thuillier: MATEC Web of conferences Vol. 408 (2257), 01075

[3] M. Conde, S. Coppieters and A. Andrade-Campos: Int. J. Mech. Sciences Vol. 264 (2024), 108813

[4] M. Dunand and D. Mohr: Int. J. Solids Struct. Vol. 47 (2010), 1130-1143

[5] A. Kacem, H. Laurent and S. Thuillier: Eng. Fracture Mech. Vol. 248 (2021), 107686

[6] A. Kumar, A. Kacem and S. Thuillier: Procedia Structural Integrity Vol. 61 (2024), 62-70

[7] A. Okada, S. Igarashi and Y. Kakazu: Fusion Eng. Design Vol. 18 (1991), 525-529

[8] T. Beerli, Christian C. Roth and D. Mohr: Acta Mater. Vol. 263 (2024), 119539

[9] Christian C. Roth, T. Tancogne-Dejean and D. Mohr: Additive Manuf. Vol. 43 (2021), 101998

[10] F. Barlat, H. Aretz, J.W. Yoon, M.E. Karabin, J.C. Brem, R.E. Dick: Int. J. Plasticity Vol. 21 (2005), 1009-1039

[11] A. Andrade-Campos, R. de-Carvalho and R.A.F. Valente: Int. J. Mech. Sci. Vol. 54 (2012), 294–305